Impact of non-ideality on mixing of hydrocarbons and water at supercritical or near-critical conditions

Citation: He, Ping; Raghavan, Ashwin and Ghoniem, Ahmed F. "Impact of Non-Ideality on Mixing of Hydrocarbons and Water at Supercritical or Near-Critical Conditions." The Journal of Supercritical Fluids 102 (July 2015): 50–65 © 2015 Elsevier B.V.

As Published: http://dx.doi.org/10.1016/j.supflu.2015.03.017

Publisher: Elsevier

Persistent URL: http://hdl.handle.net/1721.1/109935

Version: Author's final manuscript: final author's manuscript post peer review, without publisher's formatting or copy editing

Impact of Non-ideality on Mixing of Hydrocarbons and Water at Supercritical or Near-critical Conditions

Ping He[1], Ashwin Raghavan, Ahmed F. Ghoniem

Department of Mechanical Engineering, Massachusetts Institute of Technology,
Cambridge, MA 02139 United States

Abstract

The mixing of a single-component or multi-component hydrocarbon (HC) droplet in supercritical or near-critical water (SCW/NCW) is modeled. Transport, thermodynamics, and phase equilibrium sub-models are used to estimate the relevant physical properties. We use a generalized Maxwell-Stefan (MS) expression to model the multi-component mass transfer and a diffusion driving force expressed in terms of fugacity gradients to account for effects of non-ideality on mass fluxes. We compare the ideal and non-ideal diffusive driving forces for different mixing conditions and different HCs, and show that when the mixing temperature is close to or greater than the upper critical solution temperature (UCST), the non-ideal driving force model predicts a much slower mixing process and higher concentrations of the heavier HC than the ideal driving force, due to the presence of a diffusion barrier captured by the non-ideal driving force model.

Keywords: Supercritical or near-critical water, Multi-component, Maxwell-Stefan equations, Hydrocarbon droplet, Phase equilibrium

---

[1] Corresponding author. Tel.: +1 617 715 4348
Email address: phe@mit.edu (P. He)

Nomenclature

Latin letters

a, b	parameters for Peng-Robinson equation of state
A, B	constants for the PPR78 model
c	molar concentration
c_p	constant pressure specific heat
$\boldsymbol{d}$	vector of the diffusive driving force
D_{ij}	binary diffusion coefficient
D^T	thermal diffusion coefficient
f	objective function for minimization of phase equilibrium under transport constraints
$\hat{f}$	fugacity
$\boldsymbol{g}$	vector of the external body force
G	Gibbs energy
h	thermal enthalpy
J	radial mass flux
$\boldsymbol{J}$	mass flux vector
k_{ij}	binary interaction parameter
L	droplet radius
$\dot{m}$	total mass flux across an interface
M	molecular weight
n	total number of species
N_g	total number of functional groups in PPR78
P	pressure
q^*	difference of the total enthalpy flux across an interface
r	radial coordinate
R	universal gas constant
S	entropy
t	time
T	temperature
u	velocity
V	molar volume
x	molar fraction
y	mass fraction
Z	compressibility factor

Greek letters

α	occurrence of a functional group in a molecule
ω	acentric factor
ρ	density

κ	association parameter
λ	thermal conductivity
μ	kinetic viscosity
μ_r	dipole moment
$\hat{\varphi}$	fugacity coefficient
τ	viscous stress

Subscripts

0	initial value
$1, 2$	two sides of an interface
c	critical value
H	hydrocarbon
i, j	the ith or jth species
m	mixture value
s	surface value
W	water
r, θ, ϕ	spherical coordinates

Superscripts

bar	partial molar quantities
IG	ideal gas

1. Introduction

Supercritical-fluid (SCF) processes such as supercritical fluid extraction (SFE), supercritical water oxidation (SCWO), supercritical water reforming and gasification, etc. show advantages due to the special properties of SCF compared to regular fluids. Because of the strong coupling of thermodynamics, transport phenomena, and chemical kinetics (for reacting systems) in SCF processes, modeling of resulting phenomena has been the subject of a sustained effort in this field. The motivation of the current and our previous studies [1, 2] originates from an emerging refinery technology of upgrading heavy crude oils using SCW [3, 4]. In this process, heavier crude fractions in the low-value petroleum feedstocks are upgraded, and sulfur and metal contents are reduced at the same time. However, as in most thermal treatments of heavy crude oils, coking might occur. Modeling the transport and mixing process can provide a way of optimization to inhibit coking reactions.

Modeling the complete transport and mixing process in an engineering application is computationally expensive due to the coupling of turbulence, multi-phase flow, phase equilibrium, and chemical reactions. In the literature, two methodologies have been utilized: 1) modeling turbulent mixing in the absence of phase boundaries [5-13], and 2) microscale modeling of individual droplets immersed in supercritical or near-critical fluids [1, 2, 14-22]. The former applies only to fully miscible conditions. Although the latter neglects turbulence and the geometric complexity, it can provide insight into the local heat and mass transfer across the interface.

In the transport and thermodynamics studies of mixing of SCFs, mass transfer is an important process to govern species fractions at each location. Mass transfer models are based on the Fick's law or the Maxwell-Stefan (MS) expressions. Curtiss and Bird [14] proved that the generalized forms of the Fick's law and the MS expressions were equivalent, while MS expressions were simpler in multi-component cases. The given relation defines the dependency of mass flux on a diffusive driving force. The driving force can be calculated using the ideal fluid assumption, that is $-c\nabla x_i$ (where c is the concentration, and x_i is the mole fraction of species i). This ideal driving force has been commonly used in the diffusion study. However when non-ideal fluid behavior becomes important, Krishna and co-workers [15] proposed a formulation of the non-ideal diffusive driving force without derivations. Recently, Bird and co-workers [14, 16] re-derived the same formulation based on a thorough foundation using the molecular theory of gases and liquids (MTGL, 1954 [17]). The non-ideal driving force is not only related to the concentration gradient, but also to the partial fugacities.

Prior studies [1, 2, 5, 7, 9-13, 18-21] used the ideal fluid model in computing the diffusive driving force, although the equation of state, thermodynamic and transport properties, etc., took account of the non-ideality in these studies. On the other hand, the following numerical studies used the non-ideal driving force for SCF mixtures. Werling and Debenedetti [22, 23] studied the mixing of a toluene droplet with supercritical CO_2. Bellan et al. studied the mixing of H_2 and O_2 [8, 24-26], and heptane and N_2 [6], in which the fluctuation theory was used to calculate the mass and heat fluxes from a transport matrix [27]. The fluctuation theory is a generalized Fick's law approach, and is equivalent to the generalized MS approach. The derivations were documented in MTGL [17], and a recent summary can be found in [14], in which Curtiss and Bird state that the MS approach is easier for use in multi-component mixtures because the coefficients were concentration-independent, while in binary mixtures the two approaches are the same.

In prior studies using the non-ideal driving force, the importance of the non-ideality had not been explored. Our previous studies on mixing of the HC droplet and NCW/SCW using the ideal driving force revealed that the non-ideal thermodynamic properties, e.g. the upper critical solution temperature (UCST), played an important role in the mixing process. A question arises naturally: is the non-ideality also important in the mass transfer model? In this study, we answer this question and aim to reveal the importance of non-ideal driving force in the problems dealing with highly non-ideal SCF mixtures.

In this paper, we study a HC droplet, either single-component or binary-component, immersed in a bulk of NCW/SCW under a constant high pressure 24MPa. The ideal and non-ideal diffusive driving forces are compared for different HC species and mixing conditions in order to give modeling recommendation for engineering designs. The rest of the paper is organized as follows. In **Sect. 2**, the physical problem is defined, the governing equations are presented, and specially, the coupling of phase equilibrium and transport constraints developed in this study is discussed. In **Sect. 3**, the numerical methods are briefly introduced as well as the simulation configurations. In **Sect. 4**, the simulation results are presented with extensive discussions. Finally, our conclusions are presented in **Sect. 5**.

2. Formulation

The problem studied here consists of a single- or binary-HC droplet in a reservoir of supercritical or near-critical water (with specified far field conditions). Spherical symmetry is assumed, making the problem one-dimensional. The radial velocity of the droplet interface is non-zero because of the thermal expansion and the mixing of water and hydrocarbon phases.

2.1 Governing equations

The governing equations are the mass, momentum, species, energy conservation equations in 1-D spherical coordinates, and the equation of state (presented in **Sect. 2.3**)

$$\frac{\partial \rho}{\partial t}+\frac{1}{r^2}\frac{\partial}{\partial r}(r^2\rho u)=0 \tag{1}$$

$$\frac{\partial \rho u}{\partial t}+\frac{1}{r^2}\frac{\partial}{\partial r}(r^2\rho u^2)=-\frac{\partial P}{\partial r}+\frac{1}{r^2}\frac{\partial}{\partial r}(r^2\tau_{rr})+\frac{1}{r}\left(\tau_{\theta\theta}+\tau_{\phi\phi}\right) \tag{2}$$

$$\frac{\partial \rho y_i}{\partial t}+\frac{1}{r^2}\frac{\partial}{\partial r}(r^2\rho y_i u)=-\frac{1}{r^2}\frac{\partial}{\partial r}(r^2 J_i) \tag{3}$$

$$\rho c_p\frac{\partial T}{\partial t}+\rho u c_p\frac{\partial T}{\partial r}=\frac{1}{r^2}\frac{\partial}{\partial r}\left(r^2\lambda\frac{\partial T}{\partial r}\right)-\sum_i\frac{\partial \bar{h}_i}{\partial r}\frac{J_i}{M_i} \tag{4}$$

where ρ, u, P, y_i, J_i and T are the density, radial velocity, pressure, mass fraction of species i, radial mass flux of species i, and temperature; c_p, λ, $\bar{h}_i$, and M_i are the specific heat, thermal conductivity, partial molar enthalpy, and molecular weight, respectively. The details of mass flux calculations are provided in **Sect. 2.2**. The temporal and spatial coordinate variables are represented by t and $(r,\ \theta,\ \phi)$. The shear stress components are given by

$$\tau_{rr}=\frac{4}{3}\mu\left(\frac{\partial u}{\partial r}-\frac{u}{r}\right),\quad \tau_{\theta\theta}=\tau_{\phi\phi}=\frac{2}{3}\mu\left(\frac{\partial u}{\partial r}-\frac{u}{r}\right).$$

The interface between the hydrocarbon-rich phase and the water-rich phase is advected at speed u_s, which is calculated from the mass and species balance across the interface

$$\dot{m}=\rho_1(u_1-u_s)=\rho_2(u_2-u_s) \tag{5}$$

$$\rho_1(u_1 - u_s)y_{1,i} + J_{1,i} = \rho_2(u_2 - u_s)y_{2,i} + J_{2,i} \tag{6}$$

where “1” and “2” denote the conditions at the interface on the hydrocarbon-rich side and the water-rich side, respectively. The temperature at the interface T_s is determined by the energy balance at the interface

$$-\lambda_1(\nabla \mathrm{T})_1 = -\lambda_2(\nabla \mathrm{T})_2 + q^* \tag{7}$$

where $q^* = \sum_i \left[\rho_1(u_1 - u_s)y_{1,i} + J_{1,i}\right]\left(h_{2,i} - h_{1,i}\right)$. The compositions at the interface on the hydrocarbon-rich side $\{y_{1,i}\}$ and the water-rich side $\{y_{2,i}\}$ are taken as the equilibrium compositions at the local temperature and pressure, which are calculated using an equation-of-state (EoS) approach (Details are provided in **Sect. 2.3**). The fluid velocity (u_1, u_2), temperature T_s, and compositions $\{y_{1,i}, y_{2,i}\}$ at the interface are used as Dirichlet boundary conditions for solving the conservation equations on each side of the interface. Neumann and Dirichlet boundary conditions are applied at the end of the domain (denoted by “ED”), i.e. $(\partial u/\partial r)|_{ED} = 0$, $(\partial y_i/\partial r)|_{ED} = 0$, and $\mathrm{T}|_{ED} = T_{W,0}$. Spherical symmetry is enforced at the center of the droplet (denoted by “CD”), i.e. $u|_{CD} = 0$, $(\partial y_i/\partial r)|_{CD} = 0$, and $(\partial T/\partial r)|_{ED} = 0$. The droplet has an initial temperature of $T_{H,0}$ and initial compositions of $\{y_{H,i}\}$, where “H” denotes hydrocarbon and “W” denotes water in the following. The water reservoir has an initial temperature of $T_{W,0}$. $T_{H,0}$ is smaller than $T_{W,0}$, which is a technique used in engineering applications to prevent hydrocarbon coking.

2.2 Generalized Maxwell-Stefan expression for multi-component diffusion

In this study, we use MS expression to calculate diffusive flux as suggested by Curtiss and Bird [14] because the linear combination coefficients in the MS expression are concentration-independent, while those combination coefficients in the generalized Fick's law are strongly dependent on concentrations. The generalized MS equations and the diffusive driving forces are valid to arbitrary numbers of species.

2.2.1 Generalized Maxwell-Stefan equations and derivation of driving forces

Generalized MS equations [14] are

$$\sum_{j\neq i}\frac{x_i x_j}{D_{ij}}\left(\frac{\boldsymbol{J}_j}{\rho y_j}-\frac{\boldsymbol{J}_i}{\rho y_i}\right)=\boldsymbol{d}_i-\sum_{j\neq i}\frac{x_i x_j}{D_{ij}}\left(\frac{D_j^T}{\rho y_j}-\frac{D_i^T}{\rho y_i}\right)\nabla \ln T \tag{8}$$

where x_i is the mole fraction, $\mathrm{J_i}$ is the mass flux vector, D_{ij} is the binary diffusion coefficient, D_i^T is the generalized thermal diffusion coefficient, and $\boldsymbol{d}_i$ is the diffusive driving force. In this study, the thermal diffusion term in Eq. (8) is neglected. The driving force was formulated by Curtiss and Bird as

$$cRT\boldsymbol{d}_i = c x_i T\nabla\left(\frac{\bar{G}_i}{T}\right)+c x_i \bar{h}_i \nabla \ln T - y_i \nabla P - \rho y_i \boldsymbol{g}_i + y_i \sum_j \rho y_j \boldsymbol{g}_j \tag{9}$$

where c is the total molar concentration, R is the gas constant, $\bar{G}_i$ is the partial molar Gibbs energy (the chemical potential), $\bar{h}_i$ is the partial molar enthalpy, and $\boldsymbol{g}_i$ is the external body force (Note that the external force is neglected in this study). The term $T\nabla(\bar{G}_i/T)$ can be written as follows [16]

$$\begin{aligned} T\nabla\left(\frac{\bar{G}_i}{T}\right) &= \nabla\bar{G}_i - \bar{G}_i\nabla\ln T \\ &= \sum_{j=1}^{n}\left(\frac{\partial\bar{G}_i}{\partial x_j}\right)_{T,P}\nabla x_j + \left(\frac{\partial\bar{G}_i}{\partial T}\right)_{x,P}\nabla T + \left(\frac{\partial\bar{G}_i}{\partial P}\right)_{x,T}\nabla P - \bar{G}_i\nabla\ln T \\ &= \sum_{j=1}^{n}\left(\frac{\partial\bar{G}_i}{\partial x_j}\right)_{T,P}\nabla x_j - T\bar{S}_i\nabla\ln T + \bar{V}_i\nabla P - \bar{G}_i\nabla\ln T \\ &= \sum_{j=1}^{n}\left(\frac{\partial\bar{G}_i}{\partial x_j}\right)_{T,P}\nabla x_j - \bar{h}_i\nabla\ln T + \bar{V}_i\nabla P \end{aligned} \tag{10}$$

where $\bar{S}_i$ is partial molar entropy, and $\bar{V}_i$ is partial molar volume. Canceling the temperature gradient term and neglecting the external body force, the driving force becomes

$$cRT\boldsymbol{d}_i = cx_i\sum_{j=1}^{n}\left(\frac{\partial\bar{G}_i}{\partial x_j}\right)_{T,P}\nabla x_j + (cx_i\bar{V}_i - y_i)\nabla P \tag{11}$$

The partial molar Gibbs energy can be expressed using fugacity coefficients

$$\bar{G}_i = G_i^{IG} + RT\ln(x_i\hat{\varphi}_i) \tag{12}$$

where G_i^{IG} is the molar Gibbs energy of pure species *i* in the ideal gas state, and $\hat{\varphi}_i$ is the fugacity coefficient of species *i*. Substituting Eq. (12) into Eq. (11), the driving force is further reduced

$$cRT\boldsymbol{d}_i = cx_iRT\sum_{j=1}^{n}\left[\frac{\partial\ln(x_i\hat{\varphi}_i)}{\partial x_j}\right]_{T,P}\nabla x_j + (cx_i\bar{V}_i - y_i)\nabla P \tag{13}$$

In this study, the pressure gradient term is neglected, and the driving force becomes

$$\boldsymbol{d}_i = x_i\sum_{j=1}^{n}\left[\frac{\partial\ln(x_i\hat{\varphi}_i)}{\partial x_j}\right]_{T,P}\nabla x_j = \nabla x_i + x_i\sum_{j=1}^{n}\left(\frac{\partial\ln\hat{\varphi}_i}{\partial x_j}\right)_{T,P}\nabla x_j \tag{14}$$

The derivation of the generalized driving force presented above is summarized from Bird and co-workers' works [14, 16]. The same expression has been proposed by Krishna et al. [15], but without a theoretical derivation. The notations in this study are different from the cited works, and the **Appendix** shows that these notations are essentially the same. Note that our notations are easier for use in computations. The fugacity coefficients and their partial derivatives are presented in **Sect. 2.3.1-2.3.3**.

2.2.2 Driving forces for the ideal mixture

To evaluate the mass-flux model introduced in the previous subsection, we compare the above model with a simpler model, in which the concentration gradients are used as the only driving force. The driving forces in Eq. (14) based on the ideal gas assumption $\hat{\varphi}_i \equiv 1$ is

$$\boldsymbol{d}_i = \nabla x_i \tag{15}$$

The non-ideality in the generalized driving force is given by

$$\Delta\boldsymbol{d}_i^{\text{non-ideal}} = x_i \sum_{j=1}^{n} \left(\frac{\partial \ln \hat{\varphi}_i}{\partial x_j} \right)_{T,P} \nabla x_j \tag{16}$$

Note that in our previous work [2], a bulk diffusion coefficient for each species is approximately estimated using

$$D_i = \frac{1 - x_i}{\sum_{j \neq i} x_j / D_{ij}} \tag{17}$$

and the Fick's law is used to calculate the mass flux

$$\boldsymbol{J}_i = -\rho D_i \nabla y_i \tag{18}$$

In this study, MS equations (Eq. (8)) are used instead of Eq. (17)-(18). We denote the model using the ideal driving force as “the ideal fluid model” for simplicity, and correspondingly the model using the non-ideal driving force introduced in **Sect. 2.2.1** is denoted as “the non-ideal fluid model”.

2.3 Phase equilibrium and physical properties

Phase equilibrium calculation is an important part of the modeling. Most hydrocarbons have only limited miscibility in water at standard conditions (i.e., 20 $^{\circ}$C and 1 bar). However, as the temperature and pressure are raised toward the water’s critical point (374 $^{\circ}$C, 221 bar), the mutual solubility of hydrocarbons and water increases. Rich experimental data on the phase equilibrium of water and hydrocarbons exist in the literature [28-33]. However, the data are only available at certain pressures and temperatures and for a limited number of components. Specifically, LLE (liquid–liquid equilibrium) data are limited to temperatures near the mixture critical solution point.

The upper critical solution temperature (UCST) is the critical point above which there is no phase separation. Because there is no clear definitions for ternary systems or systems with more than three species and similar to what was done in our previous work, following the definitions used by Costa and Freitas [34], and Koningsveld and Staverman [35], we use the term UCST to refer a certain temperature point where a certain composition of hydrocarbons can be mixed with water in any ratio.

In our previous studies, the cubic Peng-Robinson EoS with standard van der Waals mixing rules, and the temperature-dependent binary interaction parameters (BIP) were used for the computationally efficient calculation of the LLE for hydrocarbon-water binary and ternary systems. Here we extend our model for multi-component (n>3) systems of hydrocarbons and water, and we use predictive, Peng-Robinson 1978 EoS (PPR78) model [36-38] to calculate BIPs of two species, e.g. HC-water, and HC-HC.

2.3.1 Peng-Robinson EoS with mixing rules

The cubic Peng-Robinson EoS with standard van der Waals one-fluid mixing rules [39] is given by

$$P = \frac{RT}{V - b_m} - \frac{a_m(T)}{V^2 + 2b_m V - b_m^2} \tag{19}$$

$$a_m = \sum_i \sum_j x_i x_j (1 - k_{ij}) \sqrt{a_i a_j}$$

$$b_m = \sum_i x_i b_i \tag{20}$$

where R is the universal gas constant, V is the total molar volume, and k_{ij} is the BIP. a_i and b_i are calculated from critical temperature (T_c), critical pressure (P_c), and acentric factor (ω)

$$a_i = 0.457236 \frac{R^2 T_{c,i}^2}{P_{c,i}} \left[1 + m_i \left(1 - \sqrt{\frac{T}{T_{c,i}}} \right) \right]^2$$

$$b_i = 0.0777961 \frac{RT_{c,i}}{P_{c,i}} \tag{21}$$

where for $\omega_i \leq 0.491$,

$$m_i = 0.374640 + 1.54226\omega_i - 0.26992\omega_i^2$$

and for $\omega_i > 0.491$ [40],

$$m_i = 0.379642 + 1.48503\omega_i - 0.164423\omega_i^2 + 0.0166667\omega_i^3$$

Note that for molecules with $\omega_i > 0.491$, Robinson and Peng have made a correction on m_i to achieve more accurate predictions on vapor pressures of heavy hydrocarbons.

2.3.2 LLE criteria

The fugacity coefficient calculated from the Peng-Robinson EoS and the one-fluid mixing rules is [41]

$$\begin{aligned}\ln(\hat{\varphi}_i) = &-\ln\left[Z\left(1-\frac{b_m}{V}\right)\right] + \frac{b_i}{b_m}(Z-1)\\ &-\frac{a_m}{\sqrt{8}b_mRT}\left[\frac{1}{a_m}\frac{\partial a_m}{\partial x_i} - \frac{b_i}{b_m}\right]\ln\left[\frac{V+(1+\sqrt{2})b_m}{V+(1-\sqrt{2})b_m}\right]\end{aligned} \tag{22}$$

where

$$\frac{\partial a_m}{\partial x_i} = 2\sum_j x_j(1-k_{ij})\sqrt{a_ia_j} \tag{23}$$

and $Z = PV/RT$ is the compressibility. The fugacity criteria for phase equilibrium is

$$\hat{f}_{1,i} = \hat{f}_{2,i} \text{ or } x_{1,i}\,\hat{\varphi}_{1,i} = x_{2,i}\,\hat{\varphi}_{1,i} \tag{24}$$

where “1” denotes the hydrocarbon-rich phase and “2” the water-rich phase in the equilibrium state. In a binary system, the equilibrium compositions are well defined, and can be calculated using Eq. (24) and unity conditions ($\sum x_{1,i} = \sum x_{2,i} = 1$). Unlike a binary system, there are infinite numbers of equilibrium compositions for a multi-component ($n \geq 3$) system at a given pressure and temperature. Solving the transit equilibrium compositions of a multi-component system during a transport process requires transport constraints as formulated in Eq. (5) and (6).

2.3.3 Partial derivatives of the fugacity coefficients

$\left(\frac{\partial \ln \hat{\varphi}_i}{\partial x_j}\right)_{T,P}$ is used in the non-ideal driving force accounting for the non-ideality. We derive its formulation from the Peng-Robinson EoS and the one-fluid mixing rules

$$\begin{aligned}\left(\frac{\partial \ln \hat{\varphi}_i}{\partial x_j}\right)_{T,P} &= -\frac{\frac{\partial V}{\partial x_j} - b_j}{V - b_m} - \frac{b_i b_j}{{b_m}^2}(Z-1) + \frac{b_i Z}{b_m V}\frac{\partial V}{\partial x_j} \\ &\quad - \frac{a_m\left(b_j V - b_m \frac{\partial V}{\partial x_j}\right)\left(\frac{1}{a_m}\frac{\partial a_m}{\partial x_i} - \frac{b_i}{b_m}\right)}{R_u T b_m V^*} \\ &\quad - \frac{1}{2\sqrt{2}RTb_m}\left[\frac{\partial^2 a_m}{\partial x_i \partial x_j} - \frac{b_j}{b_m}\frac{\partial a_m}{\partial x_i} - \frac{b_i}{b_m}\frac{\partial a_m}{\partial x_j} \right. \\ &\quad \left. + \frac{2a_m b_i b_j}{{b_m}^2}\right]\ln\frac{V + \left(1+\sqrt{2}\right)b_m}{V + \left(1-\sqrt{2}\right)b_m}\end{aligned} \qquad (25)$$

where

$$\frac{\partial^2 a_m}{\partial x_i \partial x_j} = 2(1 - k_{ij})\sqrt{a_i a_j} \qquad (26)$$

$$V^* = V^2 + 2b_m V - {b_m}^2 \qquad (27)$$

and

$$\frac{\partial V}{\partial x_i} = \frac{V^*\frac{\partial a_m}{\partial x_i} - \left[2a_m(V - b_m) + \frac{RTV^*}{(V-b_m)^2}\right]b_i}{2a_m(V + b_m) - \frac{RTV^*}{(V-b_m)^2}} \qquad (28)$$

2.3.4 Predictive, Peng-Robinson 1978 model

BIP k_{ij} in the one-fluid mixing rules is critical in predicting the phase equilibrium. In this study, predictive, Peng-Robinson 1978 (PPR78) model is used to calculate BIPs of

HCs and water. PPR78 model is a group contribution method used to calculate the temperature-dependent BIPs in PR-EoS with one-fluid mixing rules between any two species among alkanes, cycloalkanes, alkenes, aromatics, CO_2, H_2S, H_2, N_2, water, etc. [38]. This model has correlated a large amount of phase equilibrium experimental data of species and covered a wide temperature and pressure range. Using PPR78, a BIP is calculated using the follow equation

$$k_{ij} = \frac{-\frac{\mathcal{F}_{ij}}{2} - \left(\frac{\sqrt{a_i}}{b_i} - \frac{\sqrt{a_j}}{b_j}\right)^2}{2\frac{\sqrt{a_i a_j}}{b_i b_j}} \tag{29}$$

where

$$\mathcal{F}_{ij} = \sum_{k=1}^{N_g} \sum_{l=1}^{N_g} (\alpha_{ik} - \alpha_{jk})(\alpha_{il} - \alpha_{jl}) A_{kl} \left(\frac{298.15}{T}\right)^{(B_{kl}/A_{kl} - 1)} \tag{30}$$

$N_g = 21$ is the total number of functional groups defined in PPR78, A_{kl} and B_{kl} are constants correlated from experimental data by the authors of PPR78, and α_{ik} is the occurrence of group *k* in molecule *i*.

2.3.5 Solving the multi-component LLE under transport constraints

Infinite equilibrium points exist for multi-component LLE problems. The transport constraints are used to find the correct equilibrium point at each HC-water interface in the mixing and transport simulation. The following equation is formulated from Eq. (5) and (6)

$$\rho_1(u_1 - u_s) = \rho_2(u_2 - u_s) = \frac{J_{2,i} - J_{1,i}}{y_{1,i} - y_{2,i}} = \frac{J_{2,j} - J_{1,j}}{y_{1,j} - y_{2,j}} \tag{31}$$

Let $F_{ij} = (y_{1,j} - y_{2,j})(J_{2,i} - J_{1,i}) - (y_{1,i} - y_{2,i})(J_{2,j} - J_{1,j})$, based on which we define an objective function f of transport constraints

$$f = \sum_i \sum_{j \neq i} {F_{ij}}^2 \tag{32}$$

When $f = 0$ (note that zero is the minimum), the transport constraints (Eq. (5) and (6)) are satisfied. The Nelder-Mead method is used to minimize this objective function f among all equilibrium points according to the fugacity criteria (Eq. (24)). The minimization results fulfill Eq. (31), which is used to calculate the interfacial velocity u_s

$$u_s = u_1 - \frac{J_{2,i} - J_{1,i}}{\rho_1 (y_{1,i} - y_{2,i})} \tag{33}$$

2.3.6 Physical properties

The Tracer Liu–Silva–Macedo (TLSM) equation [42] is used to compute tracer binary diffusion coefficients, and Wesselingh and Krishna model [43] is used to construct binary diffusion coefficients based on tracer values. Chung's method [44] is used to calculate the viscosity and thermal conductivity. This method is applicable for dense fluids with pressures up to thousands of bar for a wide range of temperatures including those examined in this study. Input parameters (critical constants P_C, T_C, and V_C, acentric factor ω, dipole moment μ_r, and association parameter κ) of molecules used in this study are listed in **Table 1**. Heat capacities and molar enthalpies are calculated from departure functions using the EoS approach (formulations are listed in our previous work [1]). Ideal gas state heat capacities and molar enthalpies (not listed here) are also from

[45].

Table 1. Values of critical constants (P_C, T_C, and V_C), acentric factor (ω), dipole moment (μ_r), and association parameter κ for molecules used in this study from Yaws' Handbook [45].

	P_C (bar)	T_C (K)	V_C (cm^3/mol)	ω	μ_r	κ
Water	220.6	647.0	57.1	0.344	1.8	0.076
n-decane	21.2	618.5	603.1	0.484	0	0
n-hexadecane	14.0	723.0	593.0	0.717	0	0
n-triacontane	8.0	844.0	1805.0	1.307	0	0
Benzene	49.0	562.1	256.0	0.210	0	0
Toluene	41.4	591.8	316.0	0.264	0.360	0
1,3,5-trimethylbenzene	31.3	637.3	433.0	0.399	0.561	0
1-butylbenzene	28.9	660.5	497.0	0.394	0.369	0
1-decylnaphthalene	15.8	859.0	1070.0	0.642	0	0
1-dodecylnaphthalene	13.04	854.7	1081.5	0.807	0	0

2.3.7 Phase Equilibria in Binary HC-water systems

Table 2. UCST of binary HC-water systems at 24MPa for HC species used in this study. Measured data are from [28, 31]. Note that n-C_{10}, n-C_{16}, and n-C_{30} represent n-decane, n-hexadecane, and n-triacontane, respectively.

	n-C_{10}	n-C_{16}	n-C_{30}	benz.	toluene	trimethyl -benz.	butyl-benz.	decyl-naph.	dodecyl -naph.
Calculated UCST (K)	649.0	651.7	653.7	584.0	594.6	609.1	630.5	652.0	652.6
Measured UCST (K)	632.0	638.8	655.6	569.1	586.3	603.2	N/A	N/A	N/A

Phase equilibria of binary HC-water systems have been calculated at 24MPa for the species in **Table 1** using the fugacity criteria (Eq. (24)) and the PPR78 model (Eq. (29)-(30)). The UCSTs are listed in **Table 2** with experimental data from the literature. Because PPR78 has not included the critical locus in their datasets because of technical difficulties [38], UCST results deviate by <20K from the measurements. The phase equilibrium water compositions are shown in **Figure 1** with experimental measurements from the literature. The water mole fractions of n-decane match well with the measurements, but those of toluene have deviations of ~20% (Note that using a cubic-plus-association EoS [46], which is compatible with PPR78, improves the phase equilibrium calculations). As a group contribution method, PPR78 yields phase equilibrium results with correct trends and tolerable errors.

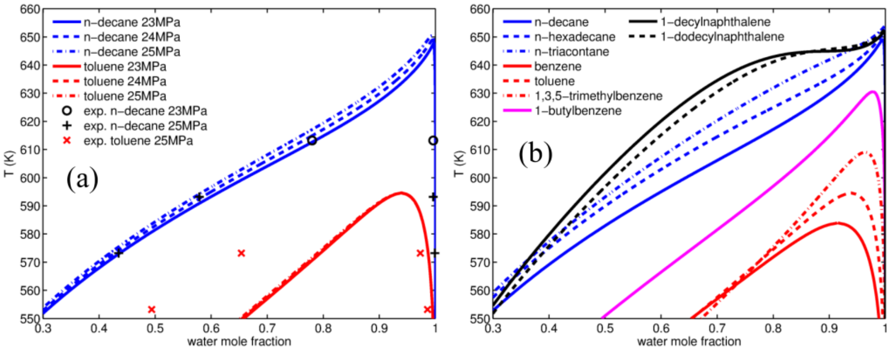

Figure 1. Equilibrium water compositions of (a) PPR78 results of n-decane and water at 23MPa (solid blue line), 24MPa (dashed blue line), and 25MPa (dash-dot blue line), toluene and water at 23MPa (solid red line), 24MPa (dashed red line), and 25MPa (dash-dot red line); and experimental data of n-decane and water at 23MPa (circle sign) and 25MPa (plus sign) [47], and experimental data of toluene and water at 25MPa (cross sign) [48]; (b) PPR78 results of binary HC-water systems at 24MPa: solid blue line for n-decane, dashed blue line for n-hexadecane, dash-dot blue line for n-triacontane, solid red line for benzene, dashed red line for toluene, dash-dot red line for 1,3,5-trimethylbenzene, solid magenta line for 1-butylbenzene, solid black line for 1-decylnaphthalene, and dashed black line for 1-dodecylnaphthalene (color figure online).

3 Numerical methods and simulation configurations

The governing equations ((1)–(4)) are solved using a 2nd order explicit Runge-Kutta scheme for temporal derivatives, 2nd order upwind schemes for advective terms, and 2nd order central difference schemes for other spatial derivatives, over the droplet domain and a surrounding domain of 10 times the droplet radius which approximates the water reservoir. The phase boundary is tracked instantly: $L(t+\Delta t)=L(t)+u_s\Delta t$, where Δt is the time step, and $L(t+\Delta t)$ and $L(t)$ are the droplet radius at a new time step and its previous time step, respectively.

A staggered uniform grid with the grid size $\Delta r = 5\mu\mathrm{m}$ is used. The time step size is $\Delta t = 10\mu\mathrm{s}$. Grid size and time-step solution independence have been tested, and these values are found to give a good balance between solution accuracy and computational economy. Time-step independence also indicates convergence at each time step for which no iteration is required for convergence. Each case requires about 10-24 hours of computer time, depending on the species number, on a single Pentium based personal computer.

4 Results and discussion

The transport and mixing processes are simulated for a single- or binary-HC droplet in a reservoir of water at supercritical or near-critical conditions. The system pressure is maintained at 24MPa. The droplet has an initial radius of $L_0 = 250\,\mu$m, and an initial temperature of $T_{H,0} = 100$°C (if not otherwise specified). The initial water temperature $T_{W,0}$ is also used as the Dirichlet boundary condition at $r = 2500\,\mu$m. Single- and binary-HC droplets have been studied to compare the results for non-ideal and ideal diffusive driving forces, and results are presented in the following.

4.1 Cases of a single-HC droplet

4.1.1 Partially miscible conditions

A 1-decylnaphthalene droplet mixing with water is studied for different initial water temperatures $T_{W,0} = 580 - 700\text{K}$. The UCST of 1-decylnaphthalene and water system is 652K. For cases of $T_{W,0} < 652\text{K}$, HC and water will have a distinct interface all the time. The case of $T_{W,0} = 620\text{K}$ is selected to represent the partially miscible conditions. The evolutions of the flow velocity, temperature and water mole fraction for the case of $T_{W,0} = 620\text{K}$ are shown in Figure 2, Figure 3 and Figure 4, respectively. The velocity profiles (*cf*. Figure 2) show that the convection is weak during the mixing process. The average velocity is $\bar{u} \sim 5\mu\text{m/s}$, and the entire process takes $t \sim 2\text{s}$. Thus the average convection distance $\bar{u}t$ is on the order of $10\mu\text{m}$, which is smaller than the droplet radius $L_0 = 250\mu\text{m}$. The velocity fields also show that the HC and water body experiences an expansion ($u > 0$) for most of the time. There is a small reverse flow of water (flow towards the droplet center) only in the early stage of mixing at $r \sim 600\mu\text{m}$. This is due to the condensed water near the HC-water interface, where the water temperature is cooled down by the HC droplet. We expect to see larger reverse flows in the water near the HC-water interface when $T_{W,0}$ is raised. Also note that the ideal and non-ideal fluid models predict close results in this case.

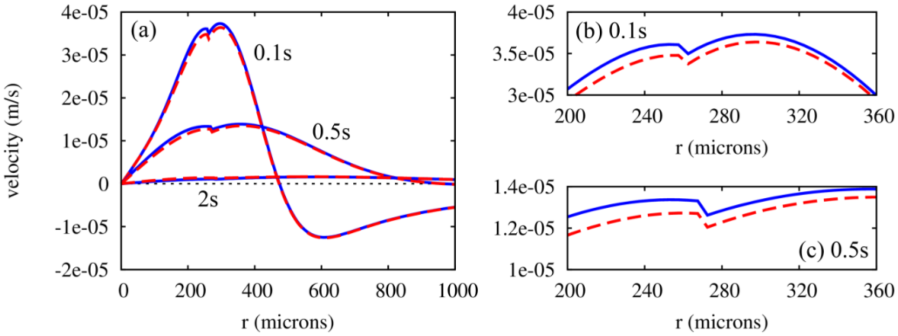

Figure 2. Evolution of flow velocity profiles in the case of a 1-decylnaphthalene droplet mixing with SCW at initial water temperature $T_{W,0} = 620\text{K}$ (results using ideal driving force in solid blue lines and those using non-ideal driving force in dashed red lines): (a) profiles at 0.1s, 0.5s and 2s, (b) an enlarged view at 0.1s, and (c) an enlarged view at 0.5s.

Because convection is weak in this case, heat conduction is the major mechanism in the heat transfer process. Temperature profiles show that water near the droplet is cooled down $\sim$30K, and the droplet's temperature increases quickly in 0.5s. Both models yield almost the same temperature profiles. Temperature profiles also show that in the early stage of the mixing process ($t = 0.1$s), the thermal diffusivities are distinctively different on the two sides of the HC-water interface.

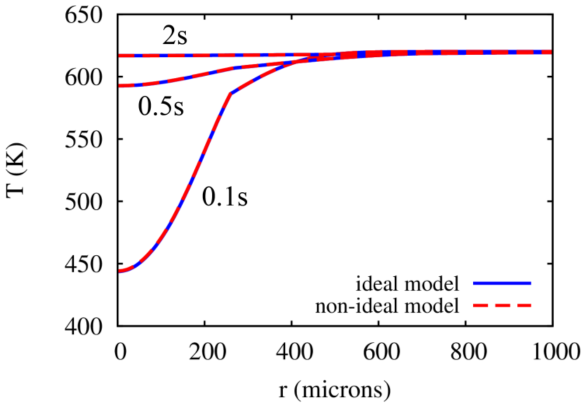

Figure 3. Evolution of temperature profiles in the case of a 1-decylnaphthalene droplet mixing with SCW at initial water temperature $T_{W,0} = 620\text{K}$ (results using ideal driving force in solid blue lines and those using non-ideal driving force in dashed red lines).

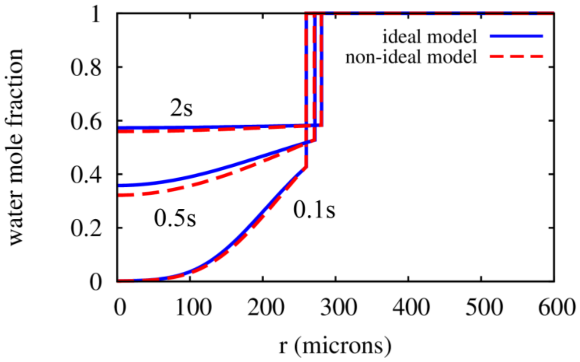

Figure 4. Evolution of water mole fraction in the case of a 1-decylnaphthalene droplet mixing with SCW at initial water temperature $T_{W,0} = 620\text{K}$ (results using ideal driving force in solid blue lines and those using non-ideal driving force in dashed red lines).

Diffusion barrier. Mole fraction results show that the non-unity fugacity has small effect on the mass diffusion in the beginning (e.g. $t = 0.1\text{s}$) and the end (e.g. $t = 2\text{s}$) of the process, and relatively large differences (~0.04 in mole fractions at $t = 0.5\text{s}$) occurs in the middle of the process. The non-ideal fluid model predicts slightly slower mass diffusion process than the ideal fluid model at $T_{W,0} = 620\text{K}$ (lower than the UCST), which indicates that the non-ideality (Eq. (16)) in the diffusion driving force acts as a diffusion barrier to slow the mixing process. Figure 5 shows that the non-ideal fluid model predicts smaller water mass flux than the ideal model in the early stage of mixing at temperatures lower than the UCST in this case, and the diffusion barrier is still small.

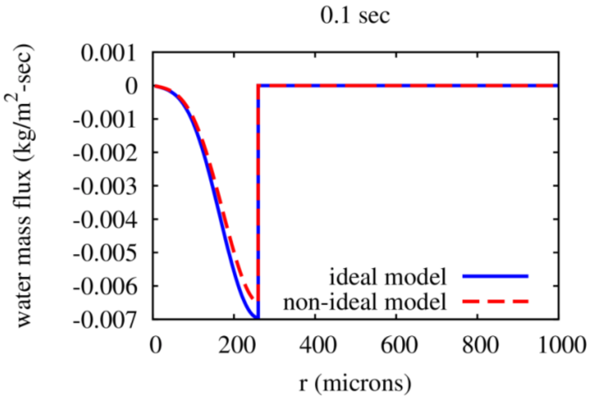

Figure 5. Water mass flux at t=0.1s in the case of a 1-decylnaphthalene droplet mixing with water at initial water temperature $T_{W,0} = 620\text{K}$ (results using ideal driving force in solid blue lines and those using non-ideal driving force in dashed red lines).

Heat transfer and mass transfer occur at similar rates as shown in the temperature and water mole fraction profiles. This is confirmed in the ratio of thermal diffusivity $\alpha = \lambda/\rho C_p$ and mass diffusivity D_{12} as shown in Figure 6. This ratio is ~ 2 in the HC droplet. Although in water this ratio is large, the heat transfer and mass transfer rates are small in the water-rich phase. The overall rates of heat transfer and mass transfer in the entire domain are on the same order of magnitude.

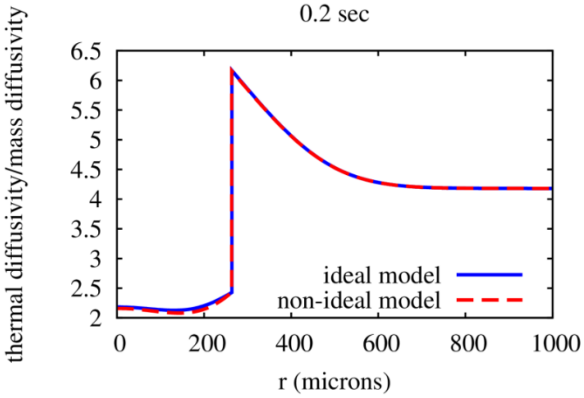

Figure 6. Ratio of thermal diffusivity and mass diffusivity at 0.2s in the case of a 1-decylnaphthalene droplet mixing with water at initial water temperature $T_{W,0} = 620\text{K}$ (results using ideal driving force in

solid blue lines and those using non-ideal driving force in dashed red lines).

4.1.2 Fully miscible conditions

In the case of $T_{W,0} = 660$K, initial water temperature is slightly above the UCST. Because the HC droplet's initial temperature is 100 ℃, the temperature at the HC-water interface is lower than the UCST for most of the time of the mixing process. The HC-water interface exists until the interfacial temperature reaches the UCST. The evolutions of the flow velocity, temperature and water mole fraction of this case are shown in Figure 7, Figure 8 and Figure 9, respectively.

The velocity profiles show that the convection becomes larger than that in the case of $T_{W,0} = 620$K, and the convection distance is on the order of 100μm. Similar to the case of $T_{W,0} = 620$K, both the HC and water experience an expansion during most of the time. However, because the difference between HC and water initial temperatures is larger, the reverse flow is $\sim$2x larger at the early stage, e.g. $t = 0.1$s. The ideal and non-ideal fluid models predict similar results in the beginning. But the difference increases with time. At $t = 0.5$ and 0.8s, the non-ideal case has smaller velocity than the ideal case, which indicates that the mole fractions and/or temperature have large differences. The jump conditions at the HC-water interface become large at $t = 0.8$ for both models, which indicate the increase of mass flux across the interface. Figure 7d shows that the ideal case reaches equilibrium earlier than the non-ideal case.

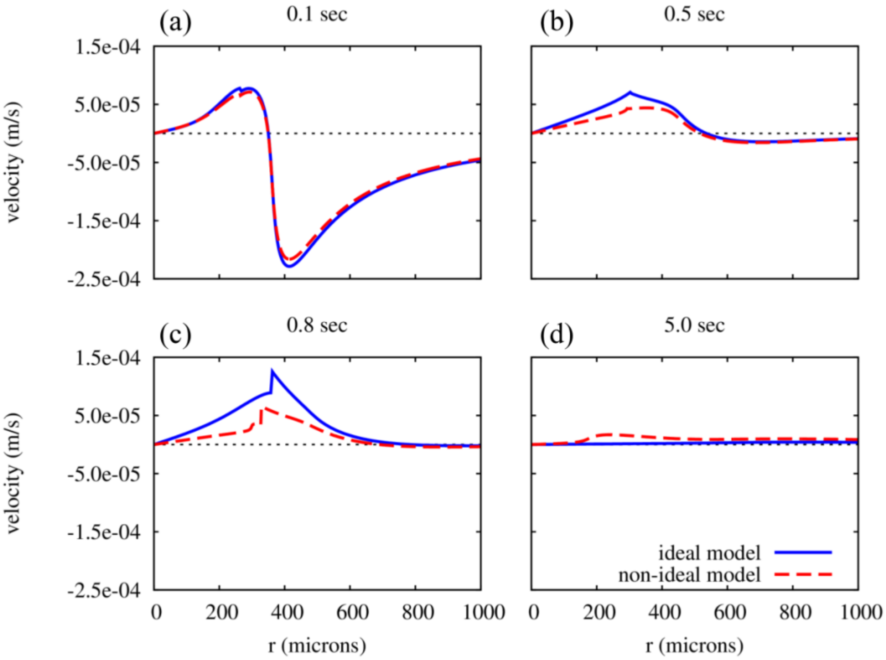

Figure 7. Evolution of flow velocity profiles in the case of a 1-decylnaphthalene droplet mixing with SCW at initial water temperature $T_{W,0} = 660\text{K}$ (results using the ideal driving force in solid blue lines and those using the non-ideal driving force in dashed red lines).

Figure 8 shows the temperature profiles for the same case. The temperature profiles are similar to those in the case of $T_{W,0} = 620\text{K}$, and both models predict similar results in the temperature.

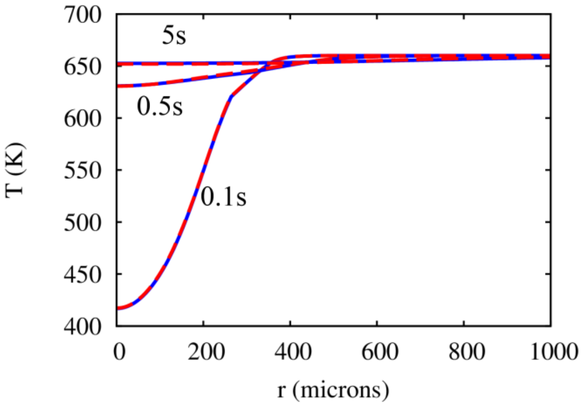

Figure 8. Evolution of temperature profiles in the case of a 1-decylnaphthalene droplet mixing with SCW at initial water temperature $T_{W,0} = 660\text{K}$ (results using the ideal driving force in solid blue lines and

those using the non-ideal driving force in dashed red lines).

Figure 9 shows the water mole fractions for the case of $T_{W,0} = 660$K. In the early stage (*cf*. Figure 9a), ideal and non-ideal fluid models yield similar results. The differences increase quickly. At $t = 0.5$s, the non-ideal fluid model predicts ~ 0.1 smaller water mole fractions than the ideal model. At $t = 0.8$s, the difference of water mole fractions increases to ~ 0.15. Moreover, the non-ideal model predicts the formation of a thin mixing front with a large gradient at $r \sim 300 \mu$m in the HC-rich phase (*cf*. Figure 10), which largely differs from that predicted by the ideal model. The reason of the formation of this mixing front is the "diffusion barrier" associated with the fugacity term in the non-ideal fluid model.

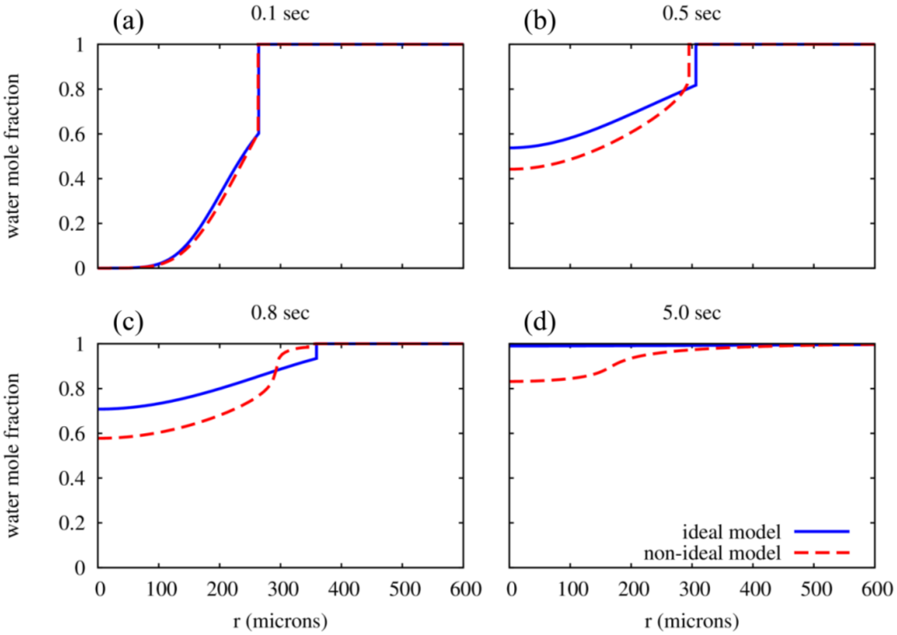

Figure 9. Evolution of water mole fraction in the case of a 1-decylnaphthalene droplet mixing with SCW at initial water temperature $T_{W,0} = 660$K (results using the ideal driving force in solid blue lines and those using the non-ideal driving force in dashed red lines).

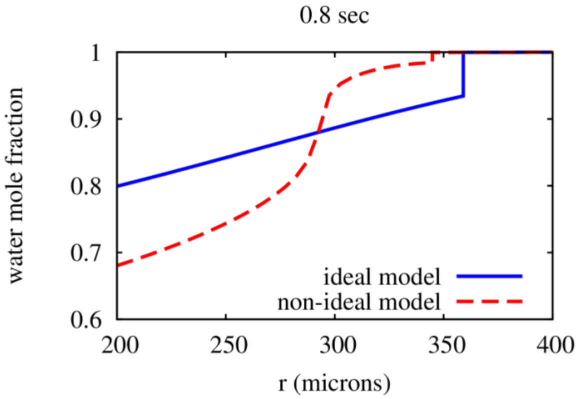

Figure 10. Water mole fraction at $t = 0.8$s in the case of a 1-decylnaphthalene droplet mixing with SCW at initial water temperature $T_{W,0} = 660\text{K}$ (enlarged view of Figure 9c). The water-HC interface locates at 359μm for the ideal model and 345μm for the non-ideal model.

The formation of a mixing front can be explained using the water mass flux profiles as shown in Figure 11. At $t = 0.5$s, the non-ideal fluid model predicts the water mass flux on the HC-rich side of the interface -0.0085kg/m^{2}s, while the ideal model shows -0.0142kg/m^{2}s, that is 40% smaller water mass flux. The non-ideality also predicts a large gradient change inside the HC-rich phase near the interface on the water mass flux profile at $t = 0.5$s. The sharp gradient in the flux profile predicted by the non-ideal fluid model directly causes water mole fractions to increase quickly in the HC-rich phase but limited in a short distance near the interface. But the diffusion in the bulk of the HC-rich phase remains slow in the non-ideal case. The difference between the diffusion at the interface and that in the HC-phase bulk initiates the formation of a large gradient in the water mole fraction near the interface ($r \sim 300\mu$m) at $t = 0.5$s. Thus a thin HC mixing front is formed.

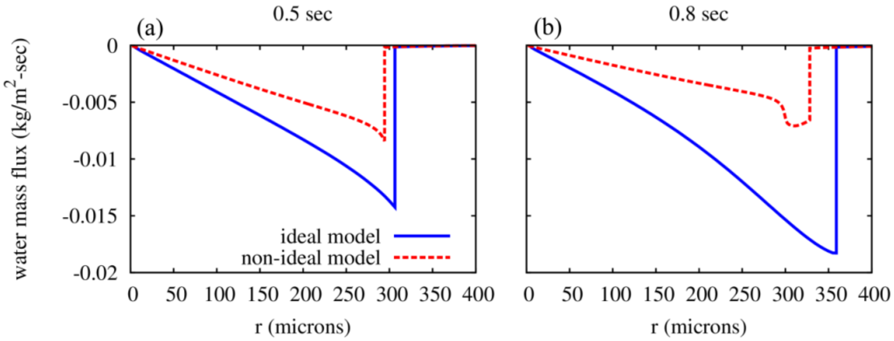

Figure 11. Water mass flux at (a) $t = 0.8$s, (b) $t = 0.8$s, and enlarged views at (c) $t = 0.5$s and (d) $t = 0.8$s in the case of a 1-decylnaphthalene droplet mixing with SCW at initial water temperature $T_{W,0} = 660$K.

Figure 11b shows that at $t = 0.8$s, the large gradient in the water mass flux profile remains close to the interface location at $t = 0.5$s ($r{\sim}300\mu$m was the interface location at $t = 0.5$s but at $t = 0.8$s it is inside the HC-rich phase – this is because the convection is small), and the non-ideal fluid model predicts mass fluxes of less than 50% as compared to the ideal model. Thus in this case, the non-ideality forms a strong diffusion barrier resisting the water diffusing into the HC-rich phase beyond the thin mixing front ($r < 300\mu$m). Figure 11b also show that the variations of the water mass flux in the thin mixing front ($300\mu\text{m} < r < 350\mu$m) become small, which indicates that in the thin mixing front, the diffusion process is negligible and the mass transfer is dominated by the slow convection.

In this case ($T_{W,0} = 660$K), the heat transfer process occurs faster than the mass transfer process, which is confirmed in Figure 12. Results show that the ratio of thermal diffusivity and mass diffusivity at $t = 0.5$ and 0.8s reaches $5-6$ at the interface on the HC side, decreases to $2-3$ in the bulk of the HC-rich phase, and remains a relatively small value of ~ 1 in the water-rich phase.

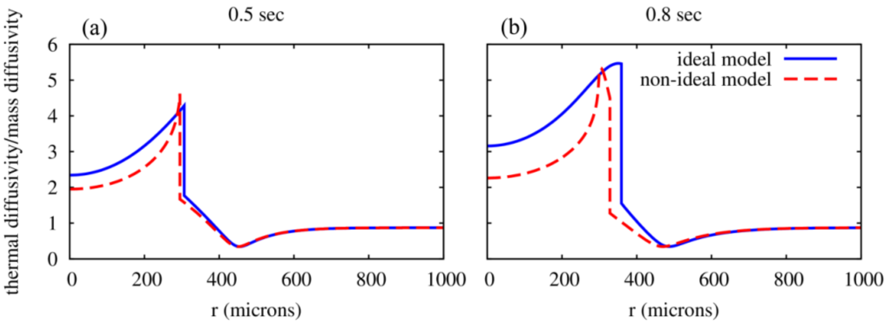

Figure 12. The ratio of thermal diffusivity and mass diffusivity at (a) $t = 0.8$s, and (b) $t = 0.8$s in the case of a 1-decylnaphthalene droplet mixing with SCW at initial water temperature $T_{W,0} = 660$K.

4.1.3 Water diffusion time t_W

The two cases discussed above show different mixings in the ideal and non-ideal models. The partially miscible case ($T_{W,0} = 620$K) show that ideal and non-ideal models yield similar results, but the fully miscible case ($T_{W,0} = 660$K) show that the non-ideal model predicts a slower diffusion process. To quantify the diffusion process, a time scale, water diffusion time t_W, is defined as the time required for the water mole fraction at the droplet center to reach 80% of its equilibrium value. Figure 13 shows the profiles of the water mole fraction at the droplet center. In the case of $T_{W,0} = 620$K, the water's equilibrium mole fraction is 60%, thus its water diffusion time t_W is defined as when the water mole fraction at the droplet center reaches 48%. Similarly in the case of $T_{W,0} = 660$K, the water's equilibrium mole fraction is 100% (fully miscible), and t_W is defined as when the value reaches 80%. The water diffusion time indicates how fast a HC-water system reaches its equilibrium state.

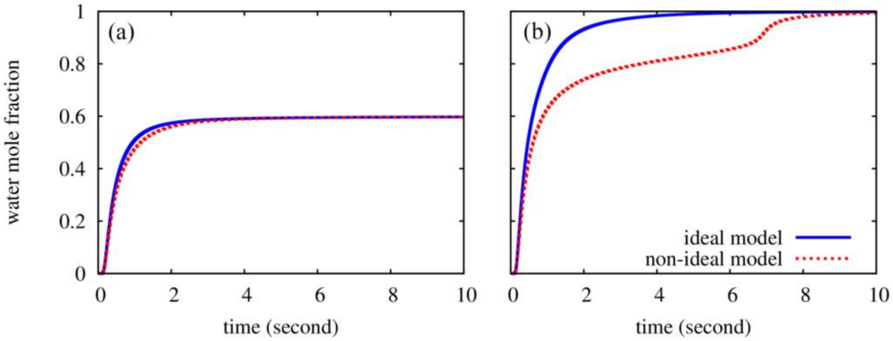

Figure 13. Evolution of water mole fractions at the droplet center for mixing of 1-decylnaphthalene droplet with water at different initial water temperatures: (a) $T_{W,0} = 620\text{K}$, and (b) $T_{W,0} = 660\text{K}$.

Figure 14a shows the water diffusion times for the case of a 1-decylnaphthalene droplet mixing with water using different water initial temperatures $T_{W,0} = 580 - 700\text{K}$. Results show that when $T_{W,0}$ below the UCST, the ideal and non-ideal models predict similar water diffusion times. When $T_{W,0}$ approaches the UCST, water diffusion time increases because *more* water can diffuse into the HC droplet. In this case, specifically when the water temperature reaches 646K, both the ideal and non-ideal models predict a sudden increase in the water diffusion time, but the non-ideal model predicts a much larger jump. As we discussed in the case of $T_{W,0} = 660\text{K}$, the non-ideal model captures a strong diffusion barrier resisting water diffusion into the HC-rich phase. The sudden increase between 644K and 646K indicates that the non-ideal diffusive force has a sudden increase. This sudden change is also revealed in the water equilibrium compositions as shown in Figure 14b. The equilibrium water composition increases quickly from 82.7% at 644K to 95.2% at 646K. The strong diffusion barrier for water is captured by both the phase equilibrium calculation and the non-ideal diffusive driving force. As $T_{W,0}$ increases past the UCST, the water diffusion time decreases as well. This is because that the temperature on the interface reaches the UCST more quickly. The maximum relative difference of water diffusion times between the two models is 70.2% at 660K.

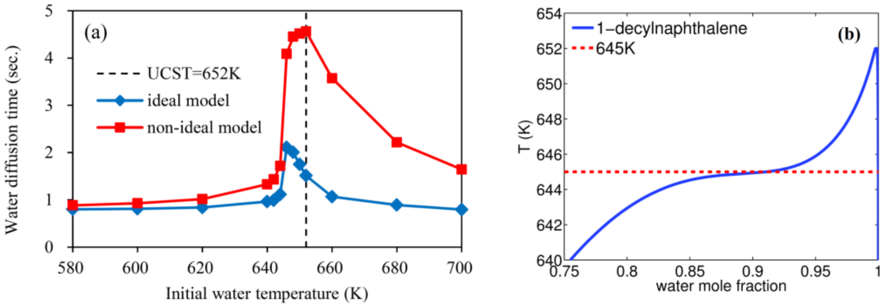

Figure 14. (a) Water diffusion times for mixing of 1-decylnaphthalene and water at different initial water temperatures $T_{W,0}$ using ideal (blue) and non-ideal (red) diffusive driving forces (the dashed line shows the UCST); (b) equilibrium water compositions in the binary mixutre of 1-decylnapthalene and water at 24MPa (an enlarged view of Figure 1b for 1-decylnapthalene), and the dashed line shows the approximate turning point at 645K.

In conclusion, the cases of a single-HC droplet show that when the system temperature is lower (e.g. 10K) than the system UCST in a HC/water mixing case, both models yield similar results. When the water temperature approaches the system UCST, the non-ideal model predicts a much slower mixing due to the strong diffusion barrier.

4.2 Cases of a binary-HC droplet (ternary systems)

In **Sect. 4.2.1**, a binary-HC, 50% benzene and 50% (mole fractions) 1-decylnaphthalene, droplet is studied for the cases in which the initial water and HC temperatures are different, and in **Sect. 4.2.2**, the same system is studied for equal initial temperatures. To investigate the effects of different HC-HC interactions on the mixing process, several HC pairs are studied in **Sect. 4.2.3**.

4.2.1 Cases of different initial temperatures

The cases studied in this subsection have the same configurations as those in **Sect. 4.1** except the ingredients of the HC droplets. The benzene and water system has a low UCST (584K), which is noted as UCST_1, and the 1-decylnaphthalene and water system's UCST (652K) is noted UCST_2. Our previous study [2] showed that the (ternary) system UCST is close to UCST_2 at this ratio, and fractionation is important when the system temperature is below the system UCST. Fractionation describes the process in which the light HC fraction, benzene, gradually diffuses into the water-rich phase, while the heavy fraction, 1-decylnaphthalene, remains in the HC-rich phase. In this subsection, first we revisit and present the fractionation in the case of $T_{W,0} = 620\mathrm{K}$; then we investigate the fully miscible conditions; and finally, water diffusion times of different initial water temperatures is presented.

Partially miscible case. Figure 15 shows mole fraction profiles for the binary-HC droplet case of $T_{W,0} = 620\mathrm{K}$. The velocity and temperature profiles are similar to those in the single-HC case of $T_{W,0} = 620\mathrm{K}$, and they are not presented here. The mole fraction profiles are also similar to the single-HC case, but with the fractionation as shown in Figure 15. The mole fraction of benzene decreases continuously during the process until it reaches ~ 0 at the end of the mixing process. The equilibrium results of this binary-HC case are the same as its corresponding single-HC case. The ideal and non-ideal fluid models yield similar results in this case. The diffusion barrier in the non-ideal model predicts lower mass fluxes (*cf*. Figure 16), and thus slower mixing process.

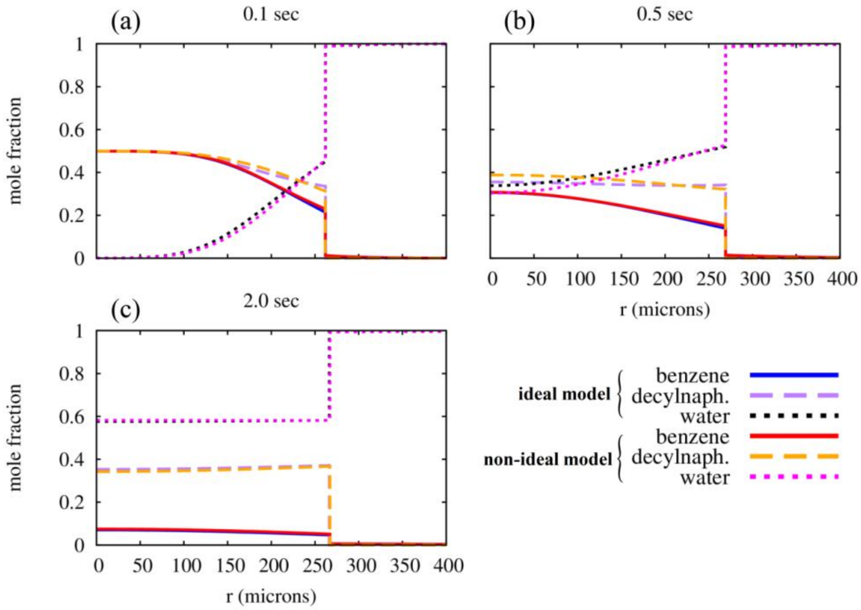

Figure 15. Evolution of mole fractions in the case of a 50% benzene and 50% 1-decylnaphthalene droplet mixing with SCW at initial water temperature $T_{W,0} = 620\text{K}$ (Results using the ideal driving force are benzene in solid blue lines, 1-decylnaphthalene in dashed purple lines, and water in dotted black lines. Those using the non-ideal driving force are benzene in solid red lines, 1-decylnaphthalene in dashed orange lines, and water in dotted magenta lines. Color figures online.)

Reverse diffusion. Figure 16 shows the mass fluxes for $\mathrm{T}_{\mathrm{W},0} = 620\mathrm{K}$ at 0.2s and 0.5s. Reverse diffusion, defined as the diffusion of a species against its concentration gradient by Toor in 1957 [49], occurs here for the heavier HC fraction 1-decylnaphthalene in both the ideal and non-ideal models. Reverse diffusion occurs in the multi-component mass transfer due to the differences in the binary diffusion coefficients. Molecules with relatively small binary diffusion coefficients, e.g. the heavier HC component 1-decylnaphthalene, tend to move slower. When the concentration gradients are not large, the smaller diffusion velocity of the heavier HC component then exhibits a reverse diffusion against its concentration gradients, because the diffusion flux is defined on the relative molecular velocity.

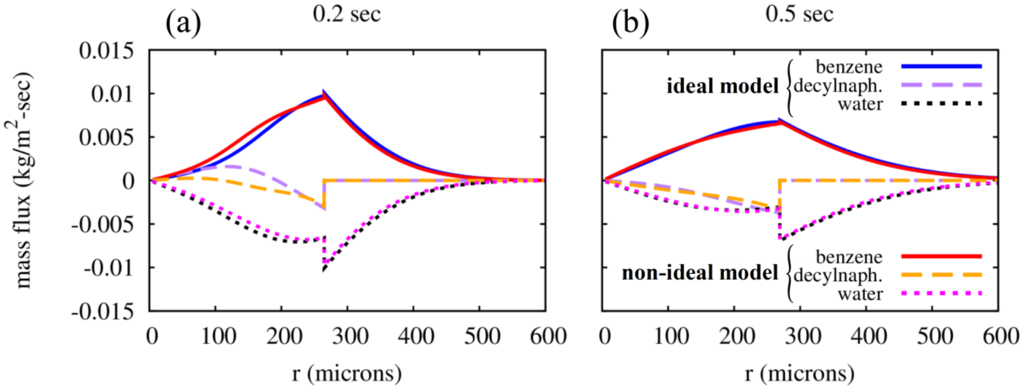

Figure 16. Evolution of species mass fluxes in the case of a 50% benzene and 50% 1-decylnaphthalene droplet mixing with SCW at initial water temperature $T_{W,0} = 620\text{K}$ (Results using the ideal driving force are benzene in solid blue lines, 1-decylnaphthalene in dashed purple lines, and water in dotted black lines. Those using the non-ideal driving force are benzene in solid red lines, 1-decylnaphthalene in dashed orange lines, and water in dotted magenta lines. Color figures online.)

We also observe that the diffusion barrier, which is caused by the non-ideality in the diffusive driving force, enhances the reverse diffusion. At and near the HC-water interface ($200\mu\text{m} < r < 250\mu\text{m}$), the ideal and non-ideal fluid models predict similar reverse diffusions. At $t = 0.2$s, the non-ideal model predicts reverse diffusions in the bulk of the HC droplet ($r < 200\mu\text{m}$), but not the ideal model. This indicates that the non-ideality tends to concentrate the heavier HC fraction toward the center of the HC-rich phase. However, the extra reverse diffusion predicted in the non-ideal model does not last long. At $t = 0.5$s, the mass flux difference between the ideal and non-ideal models vanishes and the two models yield similar mass flux results.

<u>Fully miscible case</u>. Figure 17 shows the evolution of mole fraction profiles for the

binary-HC droplet case of $T_{W,0} = 660\text{K}$. The velocity and temperature profiles not presented here because they are similar to the single-HC case. Figure 17 shows that at $t = 0.2\text{s}$, the mole fractions of 1-decylnaphthalene and water predicted by the non-ideal model are smaller than those predicted by the ideal model. The maximum difference increases to $> 6\%$ at $t = 0.5\text{s}$. However, the mole fractions of the light HC fraction benzene are almost the same for the two models during the entire process. These indicate that the non-ideality in the diffusive driving force has the least effect on the light HC fraction, which is confirmed in the mass flux profiles as shown in Figure 18.

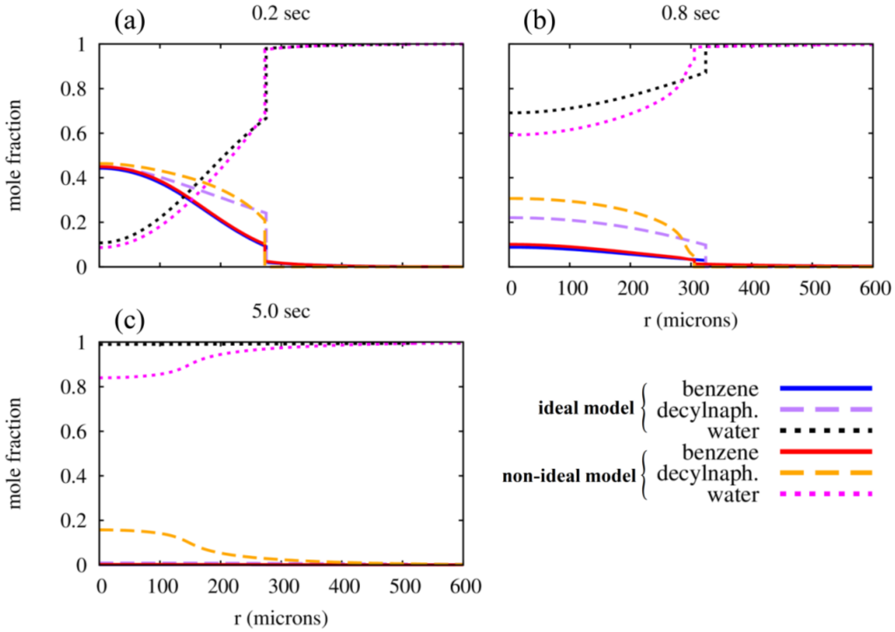

Figure 17. Evolution of mole fractions in the case of a 50% benzene and 50% 1-decylnaphthalene droplet mixing with SCW at initial water temperature $T_{W,0} = 660\text{K}$ (Results using the ideal driving force are benzene in solid blue lines, 1-decylnaphthalene in dashed purple lines, and water in dotted black lines. Those using the non-ideal driving force are benzene in solid red lines, 1-decylnaphthalene in dashed orange lines, and water in dotted magenta lines. Color figures online.)

In the case of a higher temperature $T_{W,0} = 660\text{K}$, the mass flux differences of

1-decylnaphthalene between two models last for almost the entire process. Figure 18 shows the mass fluxes at 0.2, 0.5, 0.8 and 2s. Strong reverse diffusions (-0.003 kg/m^{2}s) of 1-decylnaphthalene occurring at $r\sim200\mu$m predicted by the non-ideal at $t = 0.2$s indicate a strong diffusion barrier, while the ideal model misses this effect (positive values ~0.001 kg/m^{2}s) in the same region. The reverse diffusion of 1-decylnaphthalene predicted by the non-ideal model is -0.0025 kg/m^{2}s at the interface $r\sim250\mu$m when $t = 0.2$s, which is close to that formed in the lower $\mathrm{T}_{\mathrm{W},0}$ case ($\mathrm{T}_{\mathrm{W},0} = 620$K). In the case of $\mathrm{T}_{\mathrm{W},0} = 660$K, the reverse diffusion of 1-decylnaphthalene spreads to almost the entire HC droplet region (*cf*. the dashed orange line in Figure 18a). However, in the case of $\mathrm{T}_{\mathrm{W},0} = 620$K, the reverse diffusion of the same species decreases quickly with the radial distance, and at $r\sim200\mu$m, the reverse diffusion of 1-decylnaphthalene is only -0.0005 kg/m^{2}s (*cf*. Figure 16a).

At $t = 0.5$s, the reverse diffusion decreases due to the increase of the concentration gradient of the species. The diffusion barrier captured by the non-ideal model exhibits itself as the large gradients in the mass flux profile (*cf*. Figure 18b). The same phenomenon has been discussed in the single-HC case of $\mathrm{T}_{\mathrm{W},0} = 660$K. Because of the strong diffusion barrier, at $t = 0.5$s, a mixing front begins to form with a large gradient change in the mole fraction profiles in the non-ideal model.

At $t = 0.8$ s, the mixing front is apparently formed. The mole fraction of 1-decylnaphthalene reaches 0.05 at the interface but remains as large as 0.3 in the droplet center in the non-ideal model (*cf*. Figure 17b). Large gradients in the mole fractions of 1-decylnaphthalene and water are observe at $r \sim 290\mu$m. The same location is at 300μm in the single-HC droplet case of $\mathrm{T_{W,0}} = 660$K. The difference is caused by the large diffusion rate of benzene in the binary-HC case. Because benzene diffuses quickly from the HC droplet into the water-rich phase, the expansion of the HC droplet is slower than in the single-HC case. Due to the presence of a diffusion barrier, the non-ideal model predicts a much higher mole fraction ($> 10\%$) of 1-decylnaphthalene inside the HC droplet at $t = 0.8$s. At $t = 5$s, the mole fractions of benzene reach almost zero for both models. The mole fraction of 1-decylnaphthalene predicted by the non-ideal model now is much higher (18%).

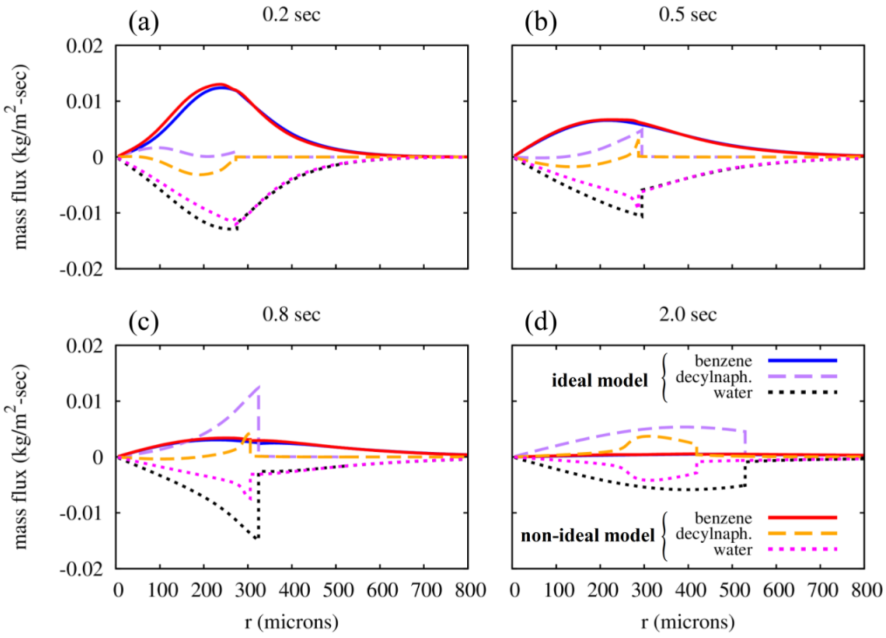

Figure 18. Evolution of mass fluxes in the case of a 50% benzene and 50% 1-decylnaphthalene droplet mixing with SCW at initial water temperature $T_{W,0} = 660$K (Results using the ideal driving force are benzene in solid blue lines, 1-decylnaphthalene in dashed purple lines, and water in dotted black lines. Those using the non-ideal driving force are benzene in solid red lines, 1-decylnaphthalene in dashed orange

lines, and water in dotted magenta lines. Color figures online.)

Water diffusion times of the binary-HC droplet case are shown in Figure 19. Similar to the single-HC droplet, the non-ideal model predicts similar water diffusion times to those predicted by the ideal model when water temperature is lower than the system UCST, but much longer times when water temperature is close to or greater than the UCST. Sudden rises of water diffusion times are observed between 642K and 646K for both models. But the gradient is sharper in the single HC component case shown in Figure 19a, because benzene works as a buffer and smears off the sudden changes of the non-ideal diffusive driving force. In addition, benzene enables the reverse diffusion of 1-decylnapthalene in both models as shown in Figure 16 and Figure 18, because reverse diffusion only occurs in multi-component mixtures and when the driving force is relatively large. The reverse diffusion of the heavier HC fraction (1-decylnaphthalene) has two main effects as shown in Figure 20: 1) it reduces the diffusion rate of water at the HC/water interface, and 2) it enhances the diffusion rate of water in the bulk of the HC droplet.

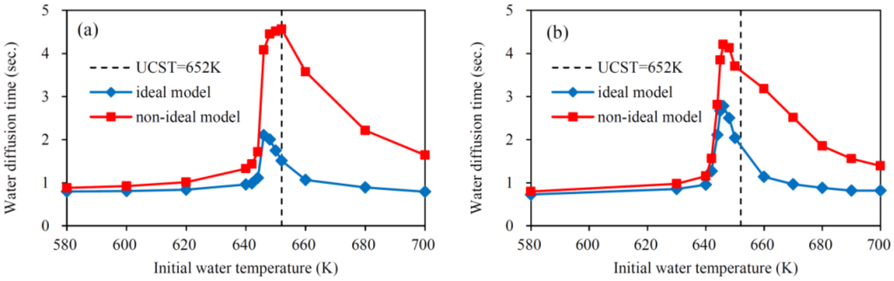

Figure 19. Water diffusion times for mixing of (a) a HC droplet of 1-decylnaphthalene (re-presenting Fig. 14a for comparison), and (b) a HC droplet of 50% benzene and 50% 1-decylnaphthalene with water at different initial water temperatures $T_{W,0}$ using ideal (blue) and non-ideal (red) diffusive driving forces (the dashed line show the UCST).

Because the ideal model does *not* compute the correct diffusion rates, the 2nd effect is not apparent, and hence the 1st effect causes the diffusion time to increase compared to the single-HC case. However the non-ideal model shows the opposite behaviors: the 1st effect is not apparent but the 2nd effect is important, and thus the diffusion time is decreased compared to the single-HC case. This comparison reaffirms the importance of the non-ideal diffusion model in accurately capturing the diffusion process of non-ideal mixtures.

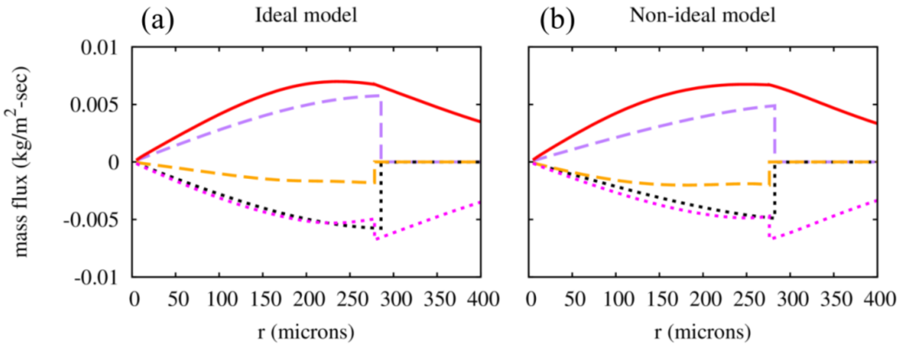

Figure 20. Mass fluxes of single- and binary-HC cases at 0.5s using (a) the ideal model, and (b) the non-ideal model: the dashed purple line is for 1-decylnaphthalene in the single-HC case, the dotted black line is for water in the single-HC case, the solid red line is for benzene in the binary-HC case, the dashed orange line is for 1-decylnaphthalene in the binary-HC case, and the dotted magenta line is for water in the binary-HC case.

4.2.2 Cases of equal initial temperatures

The same cases are also computed using equal initial temperatures for the HC and water $T = 580 - 660\text{K}$ to study the effects of temperature gradients. Similar results are found as before. The water diffusion times are presented in Figure 21. Because of the higher initial temperature of the HC droplet, the mixing times are much shorter, and no sudden increase of the water diffusion time is observed. But the same trend is captured here as regards the two models, that 1) both models yield similar results when the system temperature is lower than the UCST, 2) the non-ideal model gives larger water diffusion time than the ideal model when the system temperature is close to or greater than the UCST. The heavier HC, 1-decylnaphthalene, is also observed to highly concentrate in the HC-rich phase as that in the previous cases at high temperatures.

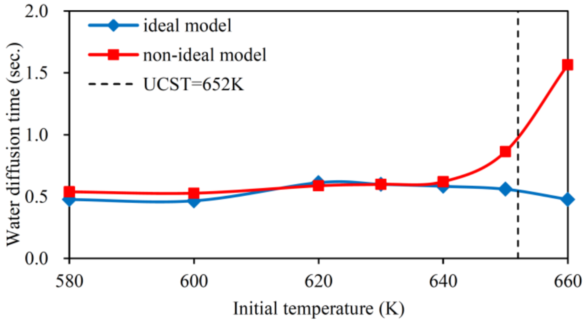

Figure 21. Water diffusion times for a 50% benzene and 50% 1-decylnaphthalene droplet mixing with water at different equal initial temperatures using ideal (blue) and non-ideal (red) diffusive driving forces (the dashed line show the UCST).

4.2.3 Cases of different HC species

We have studied the transport and mixing process of the binary and ternary systems of benzene, 1-decylnaphthalene, and water. Now we use different HC species in binary and ternary mixing cases with NCW/SCW. The mixing conditions are the same as those in **Sect. 4.2.1** except for the HC species. The HC droplet has an initial temperature of 100℃, and the initial water temperature $T_{W,0}$ varies for cases. The HC species and UCST details are listed in Table 3.

We observe that the heavy HC, e.g. n-decane in the single-HC case, and n-hexadecane in binary-HC cases as shown in Figure 22, concentrates in the HC-rich phase predicted by the non-ideal model, but the concentrating rates are lower than 1-decylnaphthalene in previous cases (*cf*. Figure 9 and Figure 17). Results indicate that HC species with lower water equilibrium compositions and larger sudden changes in phase equilibrium profiles (*cf*. Figure 1), e.g. 1-decylnaphthalene, have greater degrees of non-ideality. The concentration rate of the heavier HC as well as the increase of mixing times depend strongly on the degree of non-ideality. The UCST of n-hexadecane and water is close to that of 1-decylnaphthalene and water. But because n-hexadecane are less non-ideal than 1-decylnaphthalene, Figure 22 shows that the mixing front with large gradients in the mole fraction profiles are not formed as in the cases using 1-decylnaphthalene.

Table 3. HC species and binary UCST with water in different cases studied in **Sect. 4.2.3**

Case No.	Species 1	Species 2	$UCST_1$(K)	$UCST_2$(K)
1	$n\text{-}C_{10}$	N/A	649	N/A
2	$n\text{-}C_{10}$	$n\text{-}C_{16}$	649	651.7
3	Benzene	$n\text{-}C_{16}$	584	651.7

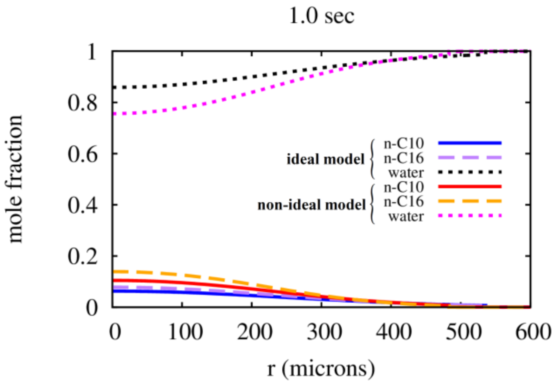

Figure 22. Mole fractions at $t = 1s$ in mixing of n-decane, n-hexadecane and water at $T_{W,0} = 660K$.

Figure 23 shows the water diffusion times calculated using the ideal and non-ideal models for these cases. Similar results are observed for all 3 cases: when the water temperature approaches the system UCST, the non-ideal model predicts higher water diffusion time. The maximum relative differences of water diffusion times between the ideal and non-ideal models are $> 30\%$ for all cases, which are caused by the diffusion barrier captured by the non-ideal diffusive driving force. However, no sudden increase of water diffusion times is found in the non-ideal model as in the previous cases using 1-decylnaphthalene (*cf*. Figure 14 and Figure 19), because benzene, n-decane and n-hexadecane have less degrees of non-ideality than 1-decylnaphthalene (Figure 1).

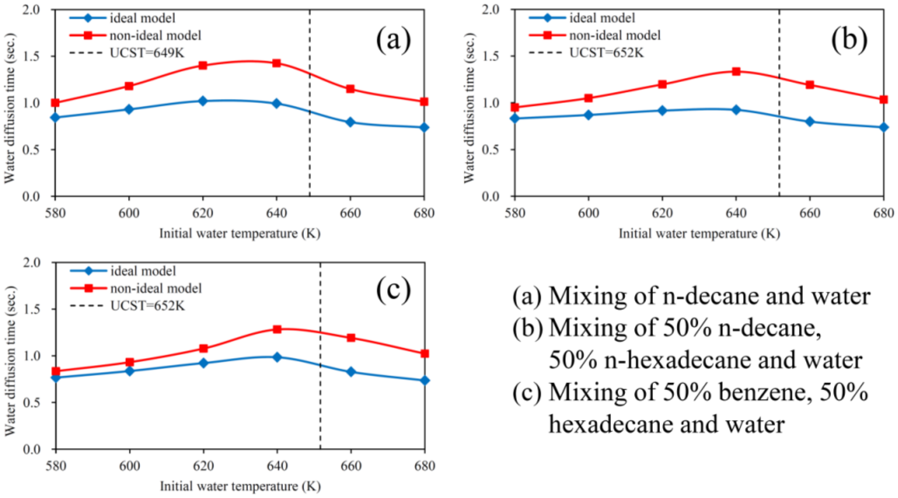

(a) Mixing of n-decane and water
(b) Mixing of 50% n-decane, 50% n-hexadecane and water
(c) Mixing of 50% benzene, 50% hexadecane and water

Figure 23. Water diffusion times for cases using different HC species.

5 Concluding remarks

The mixing process of a single-HC droplet (1-decylnaphthalene or n-decane), or a binary-HC droplet (various HC species) in a much larger reservoir of near-critical or supercritical water is examined. This study is an extension of our pervious works on a single-HC droplet and a binary-HC droplet mixing in SCW. In this study, a more accurate diffusive driving force model is used to account for the non-ideality in the mass transfer process. This non-ideal diffusive driving force is compared with the ideal driving force which was used commonly in several mass transfer problems of supercritical fluids including our previous studies. The non-ideal model gave similar mixing results to the ideal model in low temperatures (lower than the system UCST). Nevertheless, the non-ideal model predicted a much slower mixing process in high temperatures (approaching to or greater than the system UCST). Moreover, the non-ideal model predicted a significant sudden increase of mixing time for mixtures containing 1-decylnaphthalene, which has a sudden change in phase equilibrium results too. This sudden change may be a characteristic of mixing of polyaromatic hydrocarbons with NCW/SCW. Further experimental studies are needed to explore this phenomenon with polyaromatic hydrocarbons.

The non-ideal model captures an interesting mechanism in the mass transfer of highly non-ideal mixtures of HCs and water, i.e. the diffusion barrier. The term diffusion barrier was first defined by Toor in 1957 [49] to describe the zero diffusion flux of a species where its concentration gradient was non-zero in multi-component gas mixtures. But in this study, we re-define the diffusion barrier based on Toor’s concept, in which he depicted features in the multi-component diffusion process that a small change of the concentration gradient might cause a large change of the diffusion rate. We discover that by introducing the non-ideal driving force into the mass diffusion problem, even in a binary but highly non-ideal mixture, a small change of concentration gradients does cause a large change of the diffusion rate. The sharp gradient of the mass flux initially occurring in the HC-rich phase near the interface has two effects: 1) to enhance the mixing in the immediate region in the HC-rich phase near the interface, and 2) to slow down the mixing in the bulk of the HC-rich phase shortly away from the interface. Because the overall effect clearly exhibits a slower mixing process as shown in the results of both single- and binary-HC cases, we define this phenomenon as the diffusion barrier. We note that the diffusion barrier used in our study does not mean that the diffusion of water into the HC droplet is inhibited. The diffusion barrier caused by the non-ideality in the driving force strongly slows down the diffusion process.

Reverse diffusion, a species' diffusion against its concentration gradient (defined by Toor as well), was observed for the heavier HC species in binary-HC droplet cases studied here, because the heavier HC had the largest binary diffusion coefficients than the light HC species. We find that the non-ideal driving force enhances the reverse diffusion due to the presence of the diffusion barrier. However, the reverse diffusion itself does not slow down the diffusion process, and it actually enhances the mixing process slightly when the non-ideal driving force is used.

This work examined the ideal and non-ideal diffusive driving forces systematically for different temperatures and species. Results of mixing simulations indicate that whenever a mixture becomes highly non-ideal, the non-ideal driving force is a necessity to correctly describe the mass transfer process. Results show that 1) in binary mixtures of HCs and water, the non-ideality forms a diffusion barrier for water diffusion into the HCs, and increases the mixing time; 2) in ternary mixtures, the diffusion barrier of non-ideality enhances the reverse diffusion of the heavier HC, which does not only resist water diffusion, but also drives the heavier HC towards the droplet center. As a result, the heavier HC is concentrated in the HC-rich phase at high temperatures. The concentration rate of the heavier HC strongly depends on the degree of non-ideality. Our mixing results and phase equilibrium calculations show that 1-decylnaphthalene is more non-ideal than n-hexadecane, n-decane and benzene, etc.

Acknowledgment

The authors thank Saudi Aramco for supporting this work (contract number 6600023444). The support and encouragement of Dr. Ki-Hyouk Choi, Dr. Randall Field, Prof. William H. Green, and Prof. Michael T. Timko are greatly appreciated.

Appendix

In Krishna and his co-workers' works, the activity coefficient was defined as $\gamma_i(x_1, x_2, \ldots, x_{n-1})$, and $\boldsymbol{\nabla}_{T,P}\ln\gamma_i$ were calculated as

$$\boldsymbol{\nabla}_{T,P}\ln\gamma_i = \sum_{i=1}^{n-1}\left(\frac{\partial\ln\gamma_i}{\partial x_j}\right)_{T,P}\boldsymbol{\nabla}x_j \tag{34}$$

In this study, fugacity coefficients are used, which are equivalent to activity coefficients in the gases. The fugacity coefficient is defined as $\hat{\varphi}_i(x_1, x_2, \ldots, x_n)$. Because there are $\mathrm{n}-1$ independent mole fractions, the relation between the two variables are

$$\gamma_i(x_1, x_2, \ldots, x_{n-1}) = \hat{\varphi}_i(x_1, x_2, \ldots, x_{n-1}, 1 - x_1 - x_2 - \cdots - x_{n-1}) \tag{35}$$

As a result, the relation between their partial derivatives is

$$\left(\frac{\partial\ln\gamma_i}{\partial x_j}\right)_{T,P} = \left(\frac{\partial\ln\hat{\varphi}_i}{\partial x_j}\right)_{T,P} - \left(\frac{\partial\ln\hat{\varphi}_i}{\partial x_n}\right)_{T,P} \tag{36}$$

Eq. (34) is thus essentially the same as

$$\boldsymbol{\nabla}_{T,P}\ln\hat{\varphi}_i = \sum_{i=1}^{n}\left(\frac{\partial\ln\hat{\varphi}_i}{\partial x_j}\right)_{T,P}\boldsymbol{\nabla}x_j \tag{37}$$

References

[1] S. Dabiri, G. Wu, M.T. Timko, A.F. Ghoniem, Mixing of single-component hydrocarbon droplets and water at supercritical or near-critical conditions, Journal of Supercritical Fluids, 67 (2012) 29-40.

[2] G. Wu, S. Dabiri, M.T. Timko, A.F. Ghoniem, Fractionation of multi-component hydrocarbon droplets in water at supercritical or near-critical conditions, Journal of Supercritical Fluids, 72 (2012) 150-160.

[3] K. Choi, A.M. Al-Somali, M.F. Aljishi, J.H. Lee, M.R. Al-Dossary, A.K. Punetha, Supercritical water to upgrade petroluem feedstock, in: AlChE Annual Meeting, Salt Lake City, UT, 2010.

[4] A. Ates, G. Azimi, K.-H. Choi, W.H. Green, M.T. Timko, The role of catalyst in supercritical water desulfurization, Applied Catalysis B: Environmental, 147 (2014) 144-155.

[5] C.H. Oh, R.J. Kochan, T.R. Charlton, A.L. Bourhis, Thermal-hydraulic modeling of supercritical water oxidation of ethanol, Energy & Fuels, 10 (1996) 326-332.

[6] R.S. Miller, K.G. Harstad, J. Bellan, Direct numerical simulations of supercritical fluid mixing layers applied to heptane-nitrogen, Journal of Fluid Mechanics, 436 (2001) 1-39.

[7] K.S. Lieball, Numerical investigations on a transpiring wall reactor for supercritical water oxidation, in, Swiss Federal Institute of Technology Zurich, 2003.

[8] J. Bellan, Theory, modeling and analysis of turbulent supercritical mixing, Combustion Science and Technology, 178 (2006) 253-281.

[9] C. Narayanan, C. Frouzakis, K. Boulouchos, K. Prikopsky, B. Wellig, P.R. von Rohr, Numerical modelling of a supercritical water oxidation reactor containing a hydrothermal flame, Journal of Supercritical Fluids, 46 (2008) 149-155.

[10] J. Sierra-Pallares, M. Teresa Parra-Santos, J. Garcia-Serna, F. Castro, M. Jose Cocero, Numerical modelling of hydrothermal flames. Micromixing effects over turbulent reaction rates, Journal of Supercritical Fluids, 50 (2009) 146-154.

[11] J. Sierra-Pallares, D.L. Marchisio, E. Alonso, M. Teresa Parra-Santos, F. Castro, M. Jose Cocero, Quantification of mixing efficiency in turbulent supercritical water hydrothermal reactors, Chemical Engineering Science, 66 (2011) 1576-1589.

[12] A. Raghavan, A.F. Ghoniem, Simulation of supercritical water-hydrocarbon mixing in a cylindrical tee at intermediate Reynolds number: Formulation, numerical method and laminar mixing, Journal of Supercritical Fluids, 92 (2014) 31-46.

[13] A. Raghavan, A.F. Ghoniem, Simulation of supercritical water-hydrocarbon mixing in a cylindrical tee at intermediate Reynolds number: Impact of temperature difference between streams, Journal of Supercritical Fluids, 95 (2014) 325-338.

[14] C.F. Curtiss, R.B. Bird, Multicomponent diffusion, Industrial & Engineering Chemistry Research, 38 (1999) 2515-2522.

[15] G.L. Standart, R. Taylor, R. Krishna, The Maxwell-Stefan formulation of irreversible thermodynamics for simultaneous heat and mass transfer, Chemical Engineering Communications, 3 (1979) 277-289.

[16] R.B. Bird, D.J. Klingenberg, Multicomponent diffusion-A brief review, Advances in Water Resources, 62, Part B (2013) 238-242.

[17] J.O. Hirschfelder, C.F. Curtiss, R.B. Bird, U.o.W.T.C. Laboratory, Molecular theory of gases and liquids, Wiley, 1954.

[18] J.S. Shuen, V. Yang, C.C. Hsiao, Combustion of liquid-fuel droplets in supercritical conditions Combustion and Flame, 89 (1992) 299-319.

[19] V. Yang, Modeling of supercritical vaporization, mixing, and combustion processes in liquid-fueled propulsion systems, Proceedings of the Combustion Institute, 28 (2000) 925-942.

[20] T. Fadli, A. Erriguible, S. Laugier, P. Subra-Paternault, Simulation of heat and mass transfer of CO_2-solvent mixtures in miscible conditions: Isothermal and non-isothermal mixing, Journal of Supercritical Fluids, 52 (2010) 193-202.

[21] G.C. Hsiao, H. Meng, V. Yang, Pressure-coupled vaporization response of n-pentane fuel droplet at subcritical and supercritical conditions, Proceedings of the Combustion Institute, 33 (2011) 1997-2003.

[22] J.O. Werling, P.G. Debenedetti, Numerical modeling of mass transfer in the supercritical antisolvent process, Journal of Supercritical Fluids, 16 (1999) 167-181.

[23] J.O. Werling, P.G. Debenedetti, Numerical modeling of mass transfer in the supercritical antisolvent process: Miscible conditions, Journal of Supercritical Fluids, 18 (2000) 11-24.

[24] K. Harstad, J. Bellan, Interactions of fluid oxygen drops in fluid hydrogen at rocket chamber pressures, International Journal of Heat and Mass Transfer, 41 (1998) 3551-3558.

[25] K. Harstad, J. Bellan, Isolated fluid oxygen drop behavior in fluid hydrogen at rocket chamber pressures, International Journal of Heat and Mass Transfer, 41 (1998) 3537-3550.

[26] K. Harstad, J. Bellan, The Lewis number under supercritical conditions, International Journal of Heat and Mass Transfer, 42 (1999) 961-970.

[27] E. Peacock-Lopez, L. Woodhouse, Generalized transport theory and its application to binary mixtures, in: E. Matteoli, G.A. Mansoori (Eds.) Fluctuation Theory Of Mixtures, Taylor & Francis, 1990, pp. 301-333.

[28] E. Brunner, Fluid mixtures at high-pressures .9. Phase-separation and critical phenomena in 23 (normal-alkane + water) mixtures, Journal of Chemical Thermodynamics, 22 (1990) 335-353.

[29] R.E. Fornari, P. Alessi, I. Kikic, High-pressure fluid phase-equilibria - Experimental methods and systems investigated (1978-1987), Fluid Phase Equilibria, 57 (1990) 1-33.

[30] R. Dohrn, G. Brunner, High-pressure fluid-phase equilibria - Experimental methods and systems investigated (1988-1993)
Fluid Phase Equilibria, 106 (1995) 213-282.

[31] E. Brunner, M.C. Thies, G.M. Schneider, Fluid mixtures at high pressures: Phase behavior and critical phenomena for binary mixtures of water with aromatic hydrocarbons, Journal of Supercritical Fluids, 39 (2006) 160-173.

[32] R. Dohrn, S. Peper, J.M.S. Fonseca, High-pressure fluid-phase equilibria: Experimental methods and systems investigated (2000-2004), Fluid Phase Equilibria, 288 (2010) 1-54.

[33] J.M.S. Fonseca, R. Dohrn, S. Peper, High-pressure fluid-phase equilibria: Experimental methods and systems investigated (2005-2008), Fluid Phase Equilibria, 300 (2011) 1-69.

[34] R.O.R. Costa, R.F.S. Freitas, Phase behavior of poly(N-isopropylacrylamide) in binary aqueous solutions, Polymer, 43 (2002) 5879-5885.

[35] R. Koningsveld, A.J. Staverman, Determination of critical points in multicomponent polymer solutions, Journal of Polymer Science Part C: Polymer Symposia, 16 (1967) 1775-1786.

[36] J.N. Jaubert, F. Mutelet, VLE predictions with the Peng-Robinson equation of state and temperature

dependent k(ij) calculated through a group contribution method, Fluid Phase Equilibria, 224 (2004) 285-304.

[37] J.N. Jaubert, S. Vitu, F. Mutelet, J.P. Corriou, Extension of the PPR78 model (predictive 1978, Peng-Robinson EOS with temperature dependent k(ij) calculated through a group contribution method) to systems containing aromatic compounds, Fluid Phase Equilibria, 237 (2005) 193-211.

[38] J.-W. Qian, R. Privat, J.-N. Jaubert, Predicting the phase equilibria, critical phenomena, and mixing enthalpies of binary aqueous systems containing alkanes, cycloalkanes, aromatics, alkenes, and gases (N_2, CO_2, H_2S, H_2) with the PPR78 Equation of State, Industrial & Engineering Chemistry Research, 52 (2013) 16457-16490.

[39] D. Peng, D.B. Robinson, A new 2-constant equation of state, Industrial & Engineering Chemistry Fundamentals, 15 (1976) 59-64.

[40] D.B. Robinson, D.Y. Peng, The Characterization of the Heptanes and Heavier Fractions for the GPA Peng-Robinson Programs, Gas Processors Association, 1978.

[41] J.R. Elliott, C.T. Lira, Introductory Chemical Engineering: Thermodynamics, Second Edition, Prentice Hall, 2012.

[42] H.Q. Liu, C.M. Silva, E.A. Macedo, New equations for tracer diffusion coefficients of solutes in supercritical and liquid solvents based on the Lennard-Jones fluid model, Industrial & Engineering Chemistry Research, 36 (1997) 246-252.

[43] J.A. Wesselingh, R. Krishna, Mass Transfer, E. Horwood, 1990.

[44] T.H. Chung, M. Ajlan, L.L. Lee, K.E. Starling, Generalized multiparameter correlation for nonpolar and polar fluid transport-properties
Industrial & Engineering Chemistry Research, 27 (1988) 671-679.

[45] C.L. Yaws, Yaws' Critical Property Data for Chemical Engineers and Chemists, Knovel, 2012.

[46] M. Hajiw, A. Chapoy, C. Coquelet, Hydrocarbons - water phase equilibria using the CPA Equation of state with a group contribution method, Canadian Journal of Chemical Engineering, 93 (2015) 432-442.

[47] Q. Wang, K.C. Chao, Vapor liquid and liquid liquid equilibria and critical states of water + n-decane mixtures, Fluid Phase Equilibria, 59 (1990) 207-215.

[48] M. Haruki, Y. Iwai, S. Nagao, Y. Yahiro, Y. Arai, Measurement and correlation of phase equilibria for water plus hydrocarbon systems near the critical temperature and pressure of water, Industrial & Engineering Chemistry Research, 39 (2000) 4516-4520.

[49] H.L. Toor, Diffusion in three-component gas mixtures, AIChE Journal, 3 (1957) 198-207.